

Owing to uncertainties in the absolute detection efficiencies of the telescope, however, the resulting distribution was not normalized. Only the relative number of NEAs as a function of H was determined. To prevent duplication of any unknown computational errors in the Spacewatch analysis, we do not incorporate any of the software from that analysis into our new program. We also use new algorithms to predict the position versus time of the NEAs and to model the search pattern. In order to obtain comparable results, however, we preserve the method used to assign fictitious NEA orbits.

Figure 1 shows incremental values of $N(H)$ for the total observed NEA population, and for the complete population determined both from our own analysis of the NEAT data and from the earlier analysis of the Spacewatch data. Comparing the NEAT and Spacewatch results, it is apparent that the measurement of $N(H)$ is repeatable. Of the six magnitude ranges from $H = 14$ – 26 where both curves extend, the curves deviate significantly only from $H = 18$ – 20 . A linear fit to the NEAT curve in the range $H = 16$ – 22 is consistent with both data sets.

This overall correspondence cannot easily be attributed to selection effects or analysis errors. Differences in the instrumentation, survey pattern, area coverage, and the dependence of search efficiency on V and ω would lead to different selection effects for the two programs. If these were insufficiently accounted for, or if there were computational errors in the analyses, the resulting curves would have been affected differently.

The consistency between the NEAT distribution and the known population for $H < 16$ ($d > \sim 5$ km) provides additional support for our derivation. Because the known population of NEAs with $H < 16$ is nearly complete (10 of the 12 NEAs with $H < 16$ detected by NEAT were previously known, thus indicating a completeness fraction of $\sim 80\%$), any significant discrepancy would have indicated an error in the analysis.

To determine the magnitude of possible systematic errors, we repeated our simulation assuming lower and higher values for the limiting magnitude ($V = 18.9$ and $V = 19.1$) and for the phase parameter ($G = -0.03$ and $G = 0.40$), thus covering the range of uncertainty for these parameters. In all cases, the resulting $N(H)$ curves were similar to our nominal result, with the slope from $H = 14$ – 24 changing by less than 5%, and the value at $H = 18$ changing by less than 14%.

To account for possibly uncorrected or improperly corrected observational biases in our assumed orbit distribution, we repeated the simulation once more—this time choosing random orbits from the total observed population of NEAs with $H < 15$ (41 bodies as of July 1999, ref. 11). Since these larger NEAs have been surveyed to near completion, their orbits are unbiased. On the other hand, their representation of all the possible NEA orbits is sparse. Hence, any deviations from our nominal derivation for $N(H)$ represent an upper limit to the possible errors. On the basis of this comparison, we determine a systematic error of less than 3% in the average slope of $N(H)$, and less than 16% in the value at $H = 18$.

Taking into account both random and systematic errors, we thus conclude that there are 700 ± 230 NEAs with $H < 18$. This number is about half the value of previous estimates; however, given both the old and new uncertainties, we are marginally consistent with previous lower limits. This decrease of a factor of two does not substantially alter the significance of the NEA hazard. We have shown, however, that continuing, automated searches provide a reliable means to characterize the size of the NEA population. We can now confidently predict the level of effort required to survey completely those NEAs capable of global devastation.

Previous survey simulations show that the number of NEAs remaining undiscovered will diminish nearly exponentially with time, after an initial fast decay, if the detection rate of both known and unknown NEAs is held constant^{8,12}. For NEAs with high and low albedos similar to the S- and C-type asteroids that dominate the

main belt, limit $d > 1$ km corresponds to limits $H < 17.5$ and $H < 19.0$, respectively. Given the current yearly detection rates of 50 and 110 at these limits (as of the 12-month period ending June 1999, see ref. 11), and given our own estimates for the respective completeness levels of the known population ($51 \pm 17\%$ and $26 \pm 8\%$), it will take 7 ± 4 and 22 ± 14 years to reach 90% completion for these two types. Since the NEAs have a broad range of spectral types for which the associated albedos are largely spanned by C and S albedos¹³, the time to 90% completion for all NEAs larger than 1 km is probably close to the average for these two types, or 15 ± 10 years. Doubling the current world-wide detection rate would therefore lead to near completion in the next decade. □

Received 13 August; accepted 17 November 1999.

1. Shoemaker, E. M., Wolfe, R. F. & Shoemaker, C. S. in *Global Catastrophes in Earth History* (eds Sharpton, V. L. & Ward, P. D.) 155–170 (Geological Society of America, Boulder, Colorado, 1990).
2. Rabinowitz, D. L., Bowell, E., Shoemaker, E. M. & Muinonen, K. in *Hazards due to Comets and Asteroids* (ed. Gehrels, T.) 285–312 (Univ. Arizona Press, Tucson, 1994).
3. The Threat and the Opportunity of Asteroid and other Near-Earth Objects: Hearing before the Subcommittee on Space and Aeronautics of the Committee on Science (US House of Representatives) (US Government Printing Office, Washington DC, 1998).
4. Pravdo, S. H. *et al.* The near-Earth asteroid tracking (NEAT) program: an automated system for telescope control, wide-field imaging, and object detection. *Astron. J.* **117**, 1616–1633 (1999).
5. Gehrels, T. Scanning with charge-coupled devices. *Space Sci. Rev.* **58**, 347–375 (1991).
6. Helin, E. F. & Dunbar, R. S. Search techniques for near-Earth asteroids. *Vistas Astron.* **33**, 21–37 (1990).
7. Helin, E. F. & Shoemaker, E. M. The Palomar planet-crossing asteroid survey, 1973–1978. *Icarus* **40**, 321–328 (1979).
8. Harris, A. W. in *Collisional Processes in the Solar System* (eds Rickman, H. & Marov, M.) (Kluwer, Dordrecht, in the press).
9. Rabinowitz, D. L. The size distribution of the Earth-approaching asteroids. *Astrophys. J.* **407**, 412–427 (1993).
10. Rabinowitz, D. L. The size and shape of the near-Earth asteroid belt. *Icarus* **111**, 364–377 (1994).
11. Marsden, B. G. Electronic Listing at the Minor Planet Center of the IAU (cited July '99) (<http://cfa-www.harvard.edu/iau/NEO/TheNEOPage.html>).
12. Bowell, E. & Muinonen, K. in *Hazards due to Comets and Asteroids* (ed. Gehrels, T.) 149–197 (Univ. Arizona Press, Tucson, 1994).
13. McFadden, L.-A., Tholen, D. J. & Veeder, G. J. in *Asteroids II* (eds Binzel, R. P., Gehrels, T. & Matthews, M. S.) 442–467 (Univ. Arizona Press, Tucson, 1989).
14. Bowell, E. *et al.* in *Asteroids II* (eds Binzel, R. P., Gehrels, T. & Matthews, M. S.) 524–556 (Univ. Arizona Press, Tucson, 1989).

Acknowledgements

The research described in this paper was carried out by the Jet Propulsion Laboratory, California Institute of Technology, under a contract with the National Aeronautics and Space Administration.

Correspondence and requests for materials should be addressed to D. R. (e-mail: david.rabinowitz@yale.edu).

Measurement of the spatial coherence of a trapped Bose gas at the phase transition

I. Bloch, T. W. Hänsch & T. Esslinger

Sektion Physik, Ludwig-Maximilians-Universität, Schellingstrasse 4/III, D-80799 Munich, Germany, & The Max-Planck-Institut für Quantenoptik, D-85748 Garching, Germany

The experimental realization of Bose–Einstein condensates of dilute gases^{1–3} has allowed investigations of fundamental concepts in quantum mechanics at ultra-low temperatures, such as wave-like behaviour and interference phenomena. The formation of an interference pattern depends fundamentally on the phase coherence of a system; the latter may be quantified by the spatial correlation function. Phase coherence over a long range^{4–7} is the essential factor underlying Bose–Einstein condensation and

related macroscopic quantum phenomena, such as superconductivity and superfluidity. Here we report a direct measurement of the phase coherence properties of a weakly interacting Bose gas of rubidium atoms. Effectively, we create a double slit for magnetically trapped atoms using a radio wave field with two frequency components. The correlation function of the system is determined by evaluating the interference pattern of two matter waves originating from the spatially separated ‘slit’ regions of the trapped gas. Above the critical temperature for Bose–Einstein condensation, the correlation function shows a rapid gaussian decay, as expected for a thermal gas. Below the critical temperature, the correlation function has a different shape: a slow decay towards a plateau is observed, indicating the long-range phase coherence of the condensate fraction.

So far, experiments with condensed Bose gases have focused on the coherence properties of almost pure condensates, prepared at temperatures well below the critical temperature. First-order coherence of a Bose condensed gas was qualitatively shown by observing an interference pattern when two independent condensates were brought to overlap⁸. Using a spectroscopic method it has also been possible to show that the coherence length of the condensate is equal to its size^{9,10}. Aspects of second-order¹¹ and third-order coherence¹² of trapped condensates and the evolution of the relative phase between two condensates in different spin states were also explored¹³.

Here we probe the relative phase of the trapped gas between two spatially separated ‘slit’ regions. Each virtual slit region is selected by the frequency of a weak radio wave field that induces transitions between magnetically trapped and untrapped atomic states. The resulting output from the trap consists of two matter-wave beams with different energies. As a result of gravity the beams are collimated and propagate downwards. If the trapped atoms have a coherence length that spans both slit regions, a matter-wave interference pattern is observed in a snapshot of the spatial distribution of the emitted output beam, as shown in Fig. 1. The degree of spatial coherence of the trapped gas is deduced from the fringe contrast of the interference pattern, which is measured both as a function of temperature and slit separation.

Let us first consider the output wave emitted from a magnetically trapped Bose–Einstein condensate when a radio wave with a single frequency ω is applied¹⁴. The magnetic field $B(\mathbf{r})$ of our trap¹⁵ gives

rise to a harmonic potential which confines the condensate into the shape of a cigar, with its long axis oriented perpendicular to the gravitational force. Because of gravity, the minimum of the trapping potential is displaced relative to the minimum of the magnetic field ($13\ \mu\text{m}$ for our trapping parameters with a pure condensate having a radial diameter of $\sim 10\ \mu\text{m}$). Atoms are therefore predominantly transferred into the untrapped state at the intersection of the condensate with the shell that is determined by the electron spin resonance condition $1/2\mu_B|B(\mathbf{r})| = \hbar\omega$, with μ_B being the Bohr magneton¹⁴. Over the size of the trapped atomic cloud the height at which the resonance condition is fulfilled varies only by a small amount. The experimental situation is therefore well described by a one-dimensional model: in the region of the condensate the output waves can be approximated by Airy functions $\text{Ai}(\zeta)$, which are the eigenfunctions of massive particles in the gravitational potential¹⁶. These functions are characterized by an energy $E = mgz_0$, where z_0 is

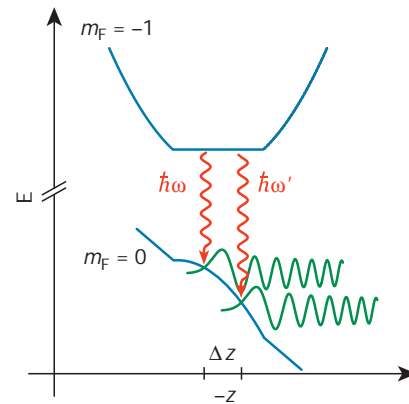


Figure 2 Measurement of the spatial coherence of a trapped Bose–Einstein condensate. A radio-wave field with two frequency components (red lines) transfers magnetically trapped atoms ($m_F = -1$) into untrapped states ($m_F = 0$). Two matter wave beams (green lines) are emitted from spatially separated locations in the trap, thereby effectively forming a double slit. The beams are accelerated by gravity and overlap outside the trap so that an interference pattern can be observed. A high contrast is detected if the trapped gas is spatially coherent over both slit regions. The harmonic potential for the trapped state and the linear potential for the untrapped state are modified by the mean field of the condensate (blue lines).

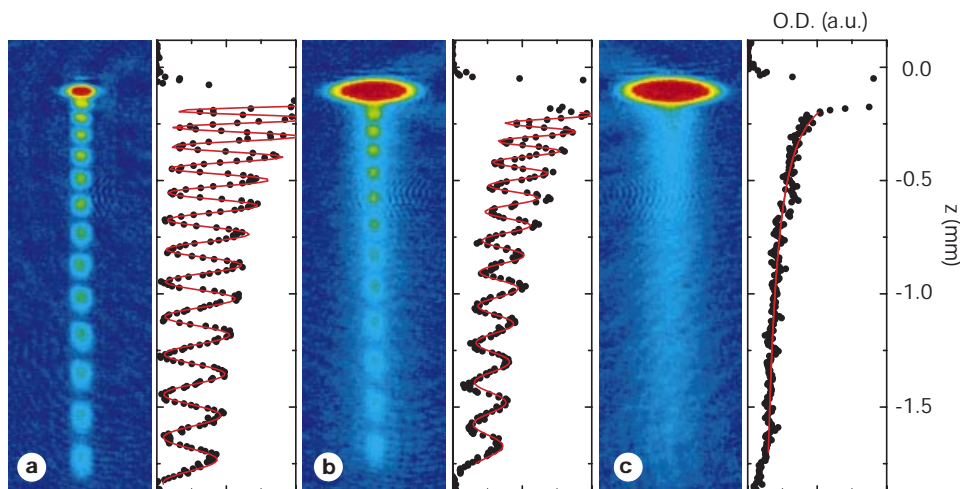


Figure 1 Interference pattern of matter-wave beams emitted from two spatially separated regions of a trapped Bose gas. **a–c**, The absorption images show the spatial distribution of the output beams for three different temperatures in false colours. For a temperature well below the critical temperature T_c the spatially uniform phase of the condensate results in a high-contrast interference pattern (**a**). When the temperature is increased to just below T_c the contrast of the interference pattern is reduced (**b**), and it vanishes

completely for temperatures above T_c (**c**). Each of the images has a size of $0.6\ \text{mm} \times 2\ \text{mm}$. The frequency difference between the two components of the radio-wave field was $1,000\ \text{Hz}$, which corresponds to a slit separation of $465\ \text{nm}$. The plots next to the images show $21\text{-}\mu\text{m}$ -wide vertical cuts through the centres of the absorption images. The horizontal axes of the plots show the optical densities. We obtain the visibilities V by using equation (1) to fit the data.

the apex of the corresponding classical trajectory, m the atomic mass and g the gravitational acceleration. The scaled parameter ζ is given by $\zeta = (z - E/mg)/l$, with a natural length scale $l = (\hbar^2/2m^2g)^{1/3}$. Outside the condensate region the asymptotic behaviour of the outgoing matter wave ϕ_{out} is given by¹⁶: $\phi_{\text{out}}(\zeta) \propto |\zeta|^{-1/4} \exp(i(2/3)|\zeta|^{3/2})$. An output wave of sharply defined energy is produced if the coupling into the untrapped state is weak and sustained for a long enough period¹⁷. Such output coupling can be described by a rate proportional to the square of the overlap integral between the output state and the trapped-state wavefunction, where the maximum contribution to the integral is localized in the region determined by the resonance condition. For our trapping parameters the mean-field interaction energy of the condensate causes only a slight distortion in the gravitational potential so that Airy functions are a good approximation for the output waves.

The radio-wave field applied in the experiment is composed of two frequencies ω and ω' , coupling the trapped condensate to two outgoing waves which have a difference in energy of $\Delta E = \hbar(\omega - \omega')$. This results in a spatial separation $\Delta z = \Delta E/mg$ between the classical turning points of the corresponding Airy functions, as illustrated in Fig. 2. Using the asymptotic approximation¹⁶, the atomic density distribution n_{out} of the output waves is given by:

$$n_{\text{out}}(z) = |\phi_{\text{out}}(\zeta) + \phi_{\text{out}}(\zeta')|^2 \propto \frac{1}{\sqrt{|z|}} \left\{ 2 + 2V \cos(q\sqrt{|z|} + (\omega - \omega')t) \right\} \quad (1)$$

Here the variable q is given by $q = m\Delta z\sqrt{2g/\hbar}$. The same interference term is obtained when two point sources for atomic de Broglie waves are considered that are positioned in the gravitational potential with a distance Δz between them¹⁸. We have additionally introduced the visibility V , which is equal to one for the case of perfect coherence and equal intensities of the two waves.

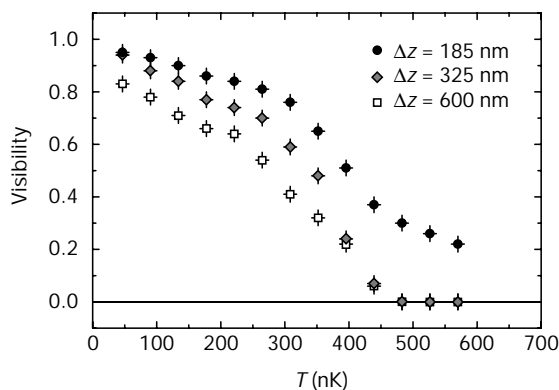


Figure 3 Spatial coherence of the Bose gas above and below the transition temperature T_c . The temperature dependency of the measured visibility is plotted for three different slit separations. Above T_c ($= 430$ nK) the visibility is zero for slit separations of 600 nm (white squares) and 325 nm (grey diamonds). A sudden increase in the visibility is detected when the temperature drops below T_c . Close to $T = 0$ the visibility reaches a maximum value of 0.95. The visibility has a qualitatively different behaviour for a slit separation of 185 nm (black circles). The visibility does not vanish at temperatures above T_c and the increase in visibility below the transition temperature is less pronounced. This is because the coherence length of the trapped gas at the transition temperature is larger than the slit separation. The slit separations of 185 nm, 325 nm and 600 nm correspond to differences of 400 Hz, 700 Hz and 1,300 Hz between the two frequency components of the radio-wave field. With increasing slit separation the fringe spacing in the interference pattern becomes smaller (see equation (1)) and the visibility is reduced by the resolution limit of our imaging system, which is $8 \mu\text{m}$. The data points displayed in Fig. 3 do not take this into account. Therefore the visibility appears to be lower for large-slit separations even for almost pure condensates at $T = 50$ nK.

The visibility becomes zero if the contrast of the observed interference pattern vanishes.

We produce samples of cold Bose gases using the same experimental set-up and a similar procedure as described in our previous work^{14,15}. In brief, rubidium-87 atoms are trapped and cooled in a magneto-optical trap. Then the atoms are optically pumped into the hyperfine ground state with the total angular momentum $F = 1$ and the magnetic quantum number $m_F = -1$. In this state the atoms are magnetically trapped and further cooled to the desired final temperature by radio-frequency-induced evaporation. A very compact magnetic trap is employed which combines the quadrupole with the Ioffe geometry¹⁵. It is placed inside a magnetic shield enclosure so that field fluctuations due to the environment are reduced to a level below 0.1 mG. The radial and axial trapping frequencies are $\omega_{\perp} = 2\pi \times 140$ Hz and $\omega_{\text{ax}} = 2\pi \times 13$ Hz, respectively. The trapped clouds we produce typically contain four million atoms at the transition temperature. To determine the temperature of the gas we apply the usual time-of-flight technique¹⁹. We estimate the absolute error of our temperature measurements to be 20 nK. The shot-to-shot fluctuations in the temperature are below this value.

The matter-wave beams are extracted from the condensate over a period of 13 ms, using a radio-wave field with two frequency components ω and ω' of the same amplitude ($0.4 \text{ mG} \pm 0.1 \text{ mG}$). After a time delay of 2 ms the magnetic trapping field is switched off and the absorption image is taken another 3 ms later. We obtain the fringe visibility V from a fit of the absorption image using equation (1), as illustrated in Fig. 1. In the experiments described below we adjusted the radio frequencies ω and ω' in such a way that the slit regions are centred around the trap minimum. Within a range of 4 kHz a simultaneous shift of both radio frequencies by the same amount results in a change in the measured visibility by less than 5%.

The fringe visibility as a function of temperature is shown in Fig. 3. Above the critical temperature T_c the gas has a coherence

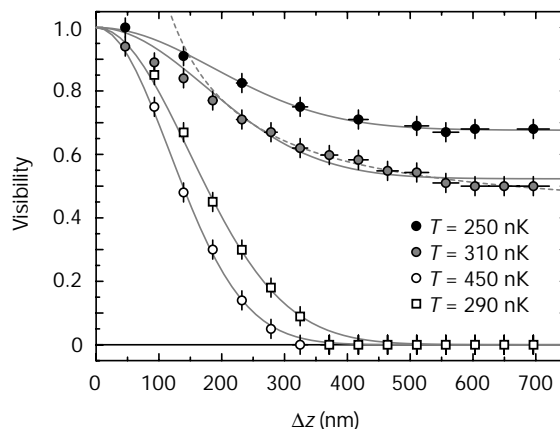


Figure 4 Spatial correlation function of a trapped Bose gas. The fringe visibility is measured as a function of slit separation for temperatures above and below the critical temperature T_c . The white circles and white squares show the measurements for thermal gases at temperatures of 450 nK and 290 nK, respectively. (To prepare a thermal gas at a temperature of 290 nK we reduced the number of atoms in the trap to 10^6). The grey data points (310 nK) and the black data points (250 nK) are the results obtained for temperatures below T_c , where the visibility decays to a nonzero value due to the long-range phase coherence of the condensate fraction. The decay of the visibility shows a longer tail than would be expected for the corresponding de Broglie wavelength of the thermal fraction. Both data sets are fitted with a gaussian function and an offset. For the temperature of 310 nK the last 11 data points are also fitted with a function proportional to $1/\Delta z$ (dashed line) and an offset. The distortion of the gravitational potential due to the mean field of the condensate leads to an uncertainty in the slit separation between 3 nm and 50 nm (see error bars). The data points displayed in the figure are corrected for the reduction in visibility which is due to the limited resolution of our imaging system.

length that is shorter than the slit separation, which was 325 nm in this case. A sudden increase in the visibility is observed when the gas is cooled below the critical temperature. For very low temperatures the visibility reaches a value of almost one. The same characteristics are observed for a slit separation of 600 nm. Qualitatively different behaviour can be seen when the slit separation is reduced to 185 nm. The slit separation is then smaller than the coherence length of the thermal gas and the interference pattern is still visible above T_c .

A more detailed physical picture is obtained from the close relation between the measured visibility V and the first-order correlation function, which is expressed by the density matrix $\rho(\mathbf{r}, \mathbf{r}')$ of the system and characterises correlations between the matter-wave field at points \mathbf{r} and \mathbf{r}' :

$$\rho(\mathbf{r}, \mathbf{r}') = \langle \hat{\Psi}^+(\mathbf{r}) \hat{\Psi}(\mathbf{r}') \rangle = \psi^*(\mathbf{r}) \psi(\mathbf{r}') + \langle \delta \hat{\Psi}^+(\mathbf{r}) \delta \hat{\Psi}(\mathbf{r}') \rangle \quad (2)$$

On the right hand side of the equation the quantized boson field operator $\hat{\Psi}(\mathbf{r})$ has been decomposed into the condensate wavefunction $\psi(\mathbf{r}) = \langle \hat{\Psi}(\mathbf{r}) \rangle$ and fluctuating part $\delta \hat{\Psi}(\mathbf{r})$. The condensate wavefunction gives rise to a long-range phase coherence and the fluctuating part describes the correlations in the excitation spectrum. For a trapped ideal gas at finite temperature the correlation function takes the form:

$$\rho(\mathbf{r}, \mathbf{r}') = \sum_k N_k u_k^*(\mathbf{r}) u_k(\mathbf{r}') \quad (3)$$

Here N_k denotes the population of the energy eigenstates u_k with energy E_k (ref. 20). The ground state describing the condensate is included in the sum.

The density distribution n_{out} of the output matter waves can be expressed in terms of the population of the trap eigenstates:

$$n_{\text{out}}(z) \propto \frac{1}{\sqrt{|z|}} \times \left\{ \sum_k N_k (|\tilde{u}_k|^2 + |\tilde{u}'_k|^2) + 2\cos(q\sqrt{|z|} + (\omega - \omega')t) \sum_k N_k \tilde{u}_k \tilde{u}'_k \right\} \quad (4)$$

The overlap integrals between the trapped and output states, which describe the coupling induced by the two frequencies ω and ω' , are given by $\tilde{u}_k = \int \text{Ai}(\zeta_k) u_k(z) dz$ and $\tilde{u}'_k = \int \text{Ai}(\zeta'_k) u_k(z) dz$. The index k of the scaled parameters ζ_k and ζ'_k indicates that the energies of the Airy functions are given by $E_k - \hbar\omega$ and $E_k - \hbar\omega'$, respectively. The main contributions to the overlap integrals are localized at the slit regions, where the trapped atoms are resonantly transferred into untrapped states. The observed visibility V (see equation (1)) can therefore be related to the density matrix and the correlation function by

$$V = \frac{2\sum_k N_k \tilde{u}_k \tilde{u}'_k}{\sum_k N_k (|\tilde{u}_k|^2 + |\tilde{u}'_k|^2)} \approx \frac{\rho(z, z')}{\rho(z, z)} \quad (5)$$

where it is assumed that the density of the trapped gas varies negligibly between the slit regions z and z' . In a numerical calculation we have compared the correlation function of a thermally populated one-dimensional harmonic oscillator with the expression for the visibility given in equation (5). We found excellent agreement for the experimental parameters, as the length scale $\sqrt{\hbar/m\omega_{\perp}}$ of the radial harmonic oscillator ground state is three times larger than the length scale l of the Airy function.

The fluctuating term in the correlation function of an interacting Bose gas at finite temperatures can be expressed in terms of the quasi-particle excitations of the condensed gas²¹. In this case the energy spectrum of the harmonic oscillator in equation (4) is replaced by the quasi-particle excitation spectrum and the overlap integrals are calculated using the mode functions of the quasi-particle states.

In a second series of experiments we have measured the fringe visibility as a function of slit separation in order to determine the correlation function of the trapped Bose gas. The data sets are displayed in Fig. 4 and show a clear distinction between condensed and non-condensed gases. For temperatures above T_c the visibility decays to zero as the slit separation increases, starting from an initial value which is close to one. We have fitted each set of data points using a gaussian curve $V = \exp(-\pi\Delta z^2/w^2)$ and obtained widths w of 294 ± 6 nm and 372 ± 8 nm. Both values are $\sim 5\%$ larger than the corresponding thermal de Broglie wavelengths λ_T of the gas, which are 278 ± 6 nm and 346 ± 12 nm. A classical ideal gas should have a correlation function of gaussian shape, with a width w given by the thermal de Broglie wavelength $\lambda_T = \sqrt{2\pi\hbar^2/(mk_B T)}$, where k_B is Boltzmann's constant. The properties of the Bose–Einstein statistics enhance the occupation of the low-energy states in a non-condensed gas resulting in a slower decay of the correlation function²⁰, as measured in our experiments.

Below the transition temperature T_c , the correlation function is modified in two significant ways. First, the correlation function decays from an initial value near unity to a plateau. The decay characterises the contribution of the non-condensed fraction to the correlation function and the visibility at the plateau is a direct measure of the condensate fraction in the slit region. At the plateau we have measured a visibility of 0.52 ± 0.03 for a temperature of 310 nK and 0.68 ± 0.03 for a temperature of 250 nK. Second, the coherence length of the non-condensed fraction is found to be substantially larger than the thermal de Broglie wavelength. We fitted both data sets with gaussian functions plus constant offsets and found widths of 428 ± 26 nm and 463 ± 16 nm for temperatures of 310 nK and 250 nK, respectively. These widths are 28% and 24% larger than the corresponding thermal de Broglie wavelengths, which are 335 ± 11 nm and 373 ± 15 nm. The slower decay of the visibility can be attributed to the long wavelength of the low-lying, phonon-type excitations of the condensed Bose gas. When the slit separation approaches the radial size of the condensate the correlation function should decay to zero, due to the finite coherence length of the condensate^{9,10}.

For a homogenous Bose gas at temperatures below T_c , the correlation function is predicted to decay towards an offset as $1/|\mathbf{r} - \mathbf{r}'|$ (ref. 22). The slit separations chosen for our measurements are small compared to the size of the condensate ground state, so that the observed behaviour should be similar to that of a homogenous system. We fitted the tail of our visibility data with a function proportional to $1/\Delta z$ and found good agreement. Furthermore, our measurements are in good qualitative agreement with numerical calculations presented in ref. 20, where the correlation function for a condensed Bose gas in a trap was calculated.

In a further experiment we have analysed the reproducibility of the interference pattern for a slit separation of 465 nm. For temperatures between 50 nK and the critical temperature we found a reproducible interference pattern, demonstrating that the condensed fraction is not fragmented into independent condensates.

Received 7 September; accepted 15 November 1999.

- Anderson, M. H., Ensher, J. R., Matthews, M. R., Wieman, C. E. & Cornell, E. A. Observation of Bose–Einstein condensation in a dilute atomic vapor. *Science* **269**, 198–201 (1995).
- Davis, K. B. *et al.* Bose–Einstein condensation in a gas of sodium atoms. *Phys. Rev. Lett.* **75**, 3969–3973 (1995).
- Bradley, C. C., Sackett, C. A. & Hulet, R. G. Bose–Einstein condensation of lithium: Observation of limited condensate number. *Phys. Rev. Lett.* **78**, 985–989 (1997).
- Penrose, O. On the quantum mechanics of helium II. *Phil. Mag.* **42**, 1373–1377 (1951).
- Penrose, O. & Onsager, L. Bose–Einstein condensation and liquid helium. *Phys. Rev.* **104**, 576–584 (1956).
- Beliaev, S. T. Application of the method of quantum field theory to a system of bosons. *J. Exp. Theor. Phys. (USSR)* **34**, 417–432 (1958).
- Yang, C. N. Concept of off-diagonal long-range order and the quantum phases of liquid He and of superconductors. *Rev. Mod. Phys.* **34**, 694–704 (1962).
- Andrews, M. R. *et al.* Observation of interference between two Bose condensates. *Science* **275**, 637–641 (1997).

9. Stenger, J. *et al.* Bragg spectroscopy of a Bose–Einstein condensate. *Phys. Rev. Lett.* **82**, 4569–4573 (1998).
10. Hagley, E. W. *et al.* Measurement of the coherence of a Bose–Einstein condensate. *Phys. Rev. Lett.* **83**, 312–315 (1999).
11. Ketterle, W. & Miesner, H. -J. Coherence properties of Bose–Einstein condensates and atom lasers. *Phys. Rev. A* **56**, 3291–3293 (1997).
12. Burt, E. A. *et al.* Coherence, correlations, and collisions: what one learns about Bose–Einstein condensates from their decay. *Phys. Rev. Lett.* **79**, 337–340 (1997).
13. Hall, D. S., Matthews, M. R., Wieman, C. E. & E. A. Cornell. Measurements of relative phase in two-component Bose–Einstein condensates. *Phys. Rev. Lett.* **81**, 1543–1546 (1998).
14. Bloch, I., Hänsch, T. W. & Esslinger, T. Atom laser with a cw output coupler. *Phys. Rev. Lett.* **82**, 3008–3011 (1999).
15. Esslinger, T., Bloch, I. & Hänsch, T. W. Bose–Einstein condensation in a quadrupole-Ioffe-configuration trap. *Phys. Rev. A* **58**, R2664–R2667 (1998).
16. Flüge, S. *Practical quantum mechanics*. 101–107 (Springer, Heidelberg, 1974).
17. Band, Y. B., Julienne P. S. & Trippenbach, M. Radio-frequency output coupling of the Bose–Einstein condensate for atom lasers. *Phys. Rev. A* **59**, 3823–3831 (1999).
18. Anderson, B. & Kasevich, M. Macroscopic quantum interference from atomic tunnel arrays. *Science* **283**, 1686–1689 (1998).
19. Ensher, J. R., Jin, D. S., Matthews, M. R., Wieman, C. E. & Cornell, E. A. Bose–Einstein condensation in a dilute gas: Measurement of energy and ground-state occupation. *Phys. Rev. Lett.* **77**, 4984–4987 (1996).
20. Naraschewski, M. & R. Glauber. Spatial coherence and density correlations of trapped Bose gases. *Phys. Rev. A* **59**, 4595–4607 (1999).
21. Fetter, A. L. Nonuniform states of an imperfect Bose gas. *Ann. Phys.* **70**, 67–101 (1972).
22. Huang, K. *Statistical Mechanics*. 2nd edn., 304 (Wiley, New York, 1987).

Acknowledgements

We thank J. Schneider, W. Zwerger and D. M. Stamper-Kurn for discussions.

Correspondence and requests for materials should be addressed to T.E. (e-mail: tie@mpq.mpg.de).

A first-order liquid–liquid phase transition in phosphorus

Yoshinori Katayama*, Takeshi Mizutani*, Wataru Utsumi*, Osamu Shimomura*, Masaaki Yamakata† & Ken-ichi Funakoshi†

* Department of Synchrotron Radiation Research, Japan Atomic Energy Research Institute, 1-1-1 Kouto, Mikazuki, Sayo, Hyogo 679-5148, Japan

† Japan Synchrotron Radiation Research Institute, 1-1-1 Kouto, Mikazuki, Sayo, Hyogo 679-5198, Japan

First-order structural phase transitions are common in crystalline solids, whereas first-order liquid–liquid phase transitions (that is, transitions between two distinct liquid forms with different density and entropy) are exceedingly rare in pure substances^{1–4}. But recent theoretical and experimental studies have shown evidence for such a transition in several materials, including supercooled water^{5–8} and liquid carbon^{9,10}. Here we report an *in situ* X-ray diffraction observation of a liquid–liquid transition in phosphorus, involving an abrupt, pressure-induced structural change between two distinct liquid forms. In addition to a known form of liquid phosphorus—a molecular liquid comprising tetrahedral P₄ molecules—we have found a polymeric form at pressures above 1 GPa. Changing the pressure results in a reversible transformation from the low-pressure molecular form into the high-pressure polymeric form. The transformation is sharp and rapid, occurring within a few minutes over a pressure range of less than 0.02 GPa. During the transformation, the two forms of liquid coexist. These features are strongly suggestive of a first-order liquid–liquid phase transition.

Phosphorus has a number of allotropes in the solid state^{11,12}. White P consists of tetrahedral P₄ molecules, whereas black P is a layered structure; red P is usually amorphous. In spite of the wide

variety of structures, the P atom is invariably threefold coordinated. Each allotrope has a different melting temperature: white P melts at 44 °C while black P and red P melt at around 600 °C (ref. 11). It is known that molten white P at 50 °C consists of P₄ molecules¹³; however, no structural study on liquid P at high temperatures has been performed except for an *ab initio* simulation study, which predicts a polymeric form at high temperatures¹⁴. Recent developments in synchrotron radiation technology and large-volume presses enable us to investigate the structures of liquids under high-pressure and high-temperature conditions^{15–18}.

We have studied the structure of the melt of black P by an *in situ* X-ray diffraction method at SPring-8, a new, third-generation synchrotron facility in Japan. Figure 1 shows the experimental paths in the pressure–temperature phase diagram of black P (refs 19, 20). The melting curve of black P has a maximum around 1 GPa, though melting temperatures of most elements increase monotonically as the pressure increases. In the region where the melting curve has a negative slope, the volume of the liquid is less than that of the solid. Hence, the occurrence of a maximum indicates an anomalous decrease in the volume of liquid with an increase in pressure: it has been related to the presence of different structural species in the liquid²¹. In the present study, X-ray diffraction data on the melt of black P were collected at several pressures below and above the melting-curve maximum.

Figure 2 shows the structure factor, *S*(*Q*), at several pressures, as obtained from X-ray diffraction data (here *Q* is the wavenumber). There is a large difference between *S*(*Q*) below and above 1 GPa. A prominent first peak around 1.4 Å⁻¹, which is characteristic of *S*(*Q*) at low pressures, disappears at high pressures. A new maximum around 2.45 Å⁻¹ appears above 1 GPa. On the other hand, *S*(*Q*) at 0.77 GPa is almost identical to that at 0.96 GPa, and *S*(*Q*) at

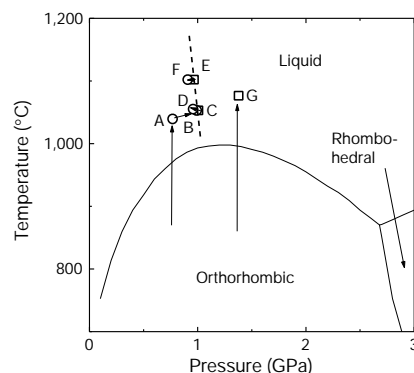


Figure 1 Experimental paths in a previously reported^{19,20} phase diagram of black P. High-pressure and high-temperature conditions were generated using a cubic-type multi-anvil press (SMAP180) installed on BL14B1 at the SPring-8 synchrotron facility. The sample assembly was similar to that used to determine the melting curve of black P (ref. 19). The sample capsule was made of BN, and the temperature was monitored by a thermocouple. When thermocouples broke down under high temperature, temperature was determined by the relation between the electric power of the heater and temperature obtained from a number of experiments under the same conditions. Pressure was determined from the lattice constant of BN (ref. 28). The absolute error in the temperature determination is about ±50 °C and that of the pressure is about ±0.1 GPa. Starting materials were either red P or black P. Red P transforms to black P under high pressure and high temperature before it melts. The samples were supplied by Akahama²⁹. The circles (squares) indicate data points where the low-pressure form (high-pressure form) was observed. The low-pressure form was obtained by melting black P at 0.77 GPa (point A). The pressure was then increased and an abrupt change in the diffraction pattern was observed between data points B and C. A reverse change was observed between data points C and D when the pressure was decreased. The high-pressure form was obtained by melting black P above 1 GPa (points E and G). The abrupt change in the diffraction pattern was observed between data points E and F. The dashed line indicates the boundary.